A new approach for the determination of the Iwan density function in modeling friction contact

A new approach for the determination of the Iwan density function in modeling friction contact

Dongwu Li[1], Daniele Botto[2], Chao Xu[1, 3*], Muzio Gola[2]

[1]*School of Astronautics, Northwestern Polytechnical University, Xi'an 710072, China*

[2] *Department of Mechanical and Aerospace Engineering, Politecnico di Torino, Turin 10129, Italy*

[3] *Qingdao R&D Institute, Northwestern Polytechnical University, Qingdao, 266200, China*

Abstract: Friction between interfaces seriously affects the dynamics of structures with joints. An accurate description of the friction behavior, usually given in the form of hysteresis loops, is then a prerequisite for a successful prediction of the dynamics of joint structures. Driven by this demand, this paper proposes a new approach in the framework of the Iwan model to better simulate the nonlinear constitutive relationship of joints. The approach derives the Iwan density function from the contact pressure distribution on the joint interface, without having to assume it like traditional Iwan-type models. Following this, the corresponding force-displacement expressions can be obtained. The proposed approach has been applied to two different contact geometries: sphere-on-sphere and flat-on-flat. For the spherical contact, comparisons between the simulated results and the analytical solutions available in the literature show perfect agreement. Moreover, the effectiveness of the approach in flat-to-flat contact has been verified by comparing the simulated hysteresis loop with the experimental counterpart.

Keywords: Mechanical joints; friction contact; Iwan model; density function; hysteresis.

* Corresponding author: chao_xu@nwpu.edu.cn
Address: Box. 127 Youyi West Road, Xi'an, Shaanxi 710072, China

1 Introduction

Jointed components are indispensable elements in mechanical systems. Due to the presence of friction at joint interfaces, the dynamic behavior of jointed structures is nonlinear and shows stiffness softening and energy dissipation. The stiffness of jointed structures depends on amplitude of oscillatory displacements, while the energy dissipation caused by friction mechanism dominates the structural damping, even reaching a 90% of the total damping [1-3]. In addition, friction could induce stick-slip vibration which results in instability of mechanical systems with friction [4-7]. A good friction model can help in the design of controllers for eliminating the frictional instability. Therefore, a reliable constitutive model capable of representing the nonlinear feature of joint mechanism is a prerequisite for predictive simulations, design and optimization of joint structures in dynamics analysis [8].

Constitutive friction models should fulfill some significant requirements [9] to be effective: i) the model must be able to describe micro/gross slip behaviors and reproduce the dependence of friction damping on the amplitude of applied loads, ii) parameters of the model should be easily estimated and iii) the model must be easily integrated into a finite element code.

In the past decades, several constitutive friction models have been developed. The Iwan model was originally developed to reproduce elastic-plastic behavior of materials and then employed to simulate the friction hysteresis behavior of joint interfaces [10, 11]. Similarly, the Valanis model originating from plasticity mechanics was used to represent the friction behavior of a bolted joint [12]. The Dahl

model was designed to simulate a symmetrical hysteresis loop observed in bearings subjected to sinusoidal excitations with small amplitudes [13, 14]. Of course, there are other contact models [15-18].

Iwan model is widely used in the field of joint structural dynamics because of its ability to describe the observed friction phenomena and the simplicity of extraction of model parameters. Many improved Iwan models [19-30] have been derived by the original model. These Iwan-type models can be grouped into two sets, according to the different modeling schemes. The first scheme is based on a combination of the framework of Iwan model with tribological approach involving rough contact [19, 20]. This modeling scheme can be regarded to be physics-based. However, it is difficult to integrate these models into dynamic analysis processes, due to the complexity of the force-displacement formulation.

The second scheme preserves the essence of the Iwan model and is based on the consideration of improving accuracy and completeness of the model. Segalman et al. [9] developed a four-parameter Iwan model that considers a power-law relation between energy dissipation and amplitude of applied load. A truncated power-law distribution with one Dirac delta function was applied to implement the representation of microslip and energy dissipation. As a supplement, Segalman et al. [21] presented an inversion of Masing models via continuous Iwan systems to address some uncommon cases in which displacement is expressed in terms of load history instead of load in terms of displacement history. The second derivative of the displacement expression is used to derive the Iwan density

function. Song et al. [22], using the experimentally observation reported in [3], employed an additional linear elastic spring in parallel with the original Iwan model to reproduce the residual stiffness during gross slip. Based on this experimental evidence, they developed an adjusted Iwan beam element to simulate the effect of bolted joints on beam structures. Similar to Song's work, Wang et al. [23] developed an improved Iwan model based on four-parameter Iwan model to describe both the residual stiffness during gross slip and the smooth transition of joint stiffness from microslip to gross slip conditions. Based on the four-parameter Iwan model and Song's finding, Li et al. [24, 25] proposed a six-parameter Iwan model to model lap joints. They used a truncated power-law distribution with two Dirac delta functions to consider two phenomena: the residual stiffness during the gross slip regime and the energy dissipation during the microslip regime. They compared simulations with experimental results, which show that the six-parameter Iwan model has good reproduction of hysteresis phenomena of lap joints. Brake [26] developed an improved Iwan model including "pinning" behavior to describe friction behavior at a bolted joint interface, in which the pinning stiffness is obtained analytically in accordance with Hertz theory [27]. This improvement can capture the contact between the bolt shank and the hole when the sliding distance between contact interfaces is greater than the gap between the bolt shank and the hole. Rajaei et al. [28] developed a generalized Iwan model, different from the abovementioned Iwan-type models. They considered the effect of the variation of normal load on tangential recovery force in two ways: the variations of distribution function of the critical sliding force and stiffness. The effects of these variations were observed on the hysteresis loops measured on a beam with frictional contact support. Recently, Li et al. [29, 30] proposed a modified Iwan model including a normal linear spring with

84 “detachment” to simulate the friction contact behavior between turbine blade and underplatform
85 damper. This model can represent both normal load variations and tangential microslip. In Ref. [30],
86 they conducted a preliminary exploration of the Iwan density function and obtained analytical force-
87 displacement expressions for line contact.
88
89 The effective modeling of joints depends on understanding and reproducing the basic physics
90 associated with a jointed interface. Although those abovementioned Iwan-type models can describe
91 the observed phenomena in some experiments, an essential fact - namely the effect of normal load
92 distribution on tangential friction behavior - has been hardly considered. Substantially, the contact
93 pressure distribution determines the motion state of a portion of contact area, either stick or slip [31].
94 In practical applications, the contact pressure distribution is influenced by the geometry of contact
95 bodies as well as roughness of surfaces which may be the main reason for the difference among some
96 measured power-law relations of energy dissipation on the amplitude of applied force [32].
97
98 This paper presents a novel approach that aims to directly calculate the Iwan density function from a
99 known or measured contact pressure distribution in the framework of the Iwan model and to further
100 better describe the friction hysteresis behavior of the joint surface. Two different contact problems:
101 spherical contact and flat contact, are treated separately. Furthermore, the effectiveness of the
102 approach is verified by comparison with analytical solutions and experimental results. The paper is
103 organized as follows. Section 2 describes the paradigm behind the proposed modeling approach and
104 introduces the corresponding parameter estimation method. The proposed model is applied to two

105 different contact geometries. Section 3 shows the case of a sphere-on-sphere contact. Results of the
106 simulation, summarized by hysteresis loops, are compared with the analytical solution given by
107 Mindlin [31]. Section 4 deals with a flat-on-flat contact and this case is used to validate the model by
108 comparing simulated results with experimental hysteresis loops. Section 5 closes the paper
109 discussing the overall approach and presenting the main conclusions.

Nomenclature			
k_t	tangential contact stiffness	G	shear modulus
n	number of Jenkins elements	T_m	amplitude of tangential force
f_i^*	critical sliding force on the i^{th} element	W	dissipated energy per cycle
φ	density function	r	distance from the contact center
Δ	range of critical sliding force	n_{eq}	normal force per contact width
μ	friction coefficient	γ	proportional coefficient
N	normal load	p_m	mean contact pressure
T	tangential friction force	w	width of the plate
δ	tangential elative displacement	h	thickness of the plate
δ_m	amplitude of relative displacement	lb	lower bound of the integral
p	distribution function of contact pressure	ub	upper bound of the integral
x, y	spatial coordinates	α	residual stiffness coefficient
a	size of contact area	T_{norm}	normalized tangential force
$t,\ t'$	tangential sliding stress (traction)	δ_{norm}	normalized relative displacement
p_0	maximum contact pressure	DF	density function
ϑ	Poisson's ratio	SD	sliding direction

110

2 Modeling approach

In this section, the Iwan model is briefly reviewed and the importance of the Iwan density function (DF) is emphasized. Then we put forward a novel approach that can explicitly determine the Iwan DF from the pressure distribution on the contact surface. This approach gives a physics-based explanation of the DF and does not introduce new parameters.

2.1 The density function of Iwan model

The Iwan model [10] consists of Jenkins elements [33] in a parallel as shown in Fig. 1(a). A Jenkins element is an ideal piecewise unit which can reproduce either slip or stick. Each element is composed of a linear spring whose stiffness is k_t/n and a Coulomb slider with a critical sliding force f_i^*/n. The stiffness k_t is the total tangential stiffness, f_i^* is the critical sliding force on the i^{th} element and n is the number of Jenkins elements. The critical sliding force is the tangential force on a single element at the onset of sliding. It should be noted that the critical sliding force is typically different for each element. According to [10], the critical sliding force on each element can be represented by a density function $\varphi(f^*)$ where "$\varphi(f^*)df^*$ *is the fraction of total number of elements having* $f^* \le f_i^* \le f^*+\mathrm{d}f^*$". The original Iwan model assumes a uniform DF $\varphi(f^*)=1/\Delta$, as indicated in Fig. 1(b), where μ is the friction coefficient, N the normal load and Δ the range of f^*.

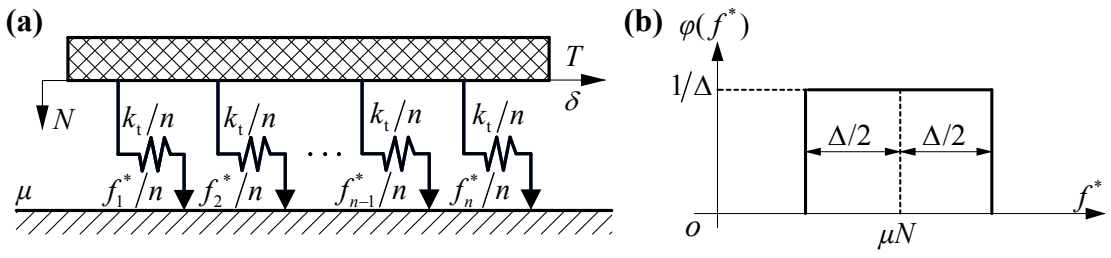

Fig. 1. (a) Scheme of the Iwan model, (b) a uniform density function of the critical sliding force.

The total tangential force results from two groups of elements: those elements which are in slip or yield state and the elements which are unyielded or in stick state. For a small-amplitude monotonic loading case, the force-displacement relation (also called backbone function) is defined as

$$T(\delta) = \int_0^{k_t\delta} f^* \varphi(f^*) df^* + k_t\delta \int_{k_t\delta}^{\infty} \varphi(f^*) df^*. \quad (1)$$

where T is the tangential force and δ the relative displacement. Increasing the relative displacement increases the tangential force. All the elements will be in a slip state once the tangential force becomes larger than the limit force associated to a given friction coefficient, μN. From Eq. (1), it can be seen that the DF is of great importance, which directly relates the total tangential force to the relative displacement.

For a cyclic load, the tangential force during unloading is,

$$T(\delta) = \int_0^{\frac{k_t(\delta_m - \delta)}{2}} -f^* \varphi(f^*) df^* + \int_{\frac{k_t(\delta_m - \delta)}{2}}^{k_t\delta_m} [f^* - k_t(\delta_m - \delta)] \varphi(f^*) df^* + k_t\delta \int_{k_t\delta_m}^{\infty} \varphi(f^*) df^*, \quad (2)$$

where δ_m is the maximum displacement reached at the end of the loading phase. The expression of the tangential force for reloading can be deduced in a similar way. Eq. (2) is based on the Masing's hypothesis [9, 21] and further details can be found in Ref. [10, 11].

The original Iwan model [10] uses three parameters (stiffness, total "yield force", and the range of the yield force) to describe the relationship between the force and the displacement. The ratio of the

146 force range over the yield force is related to the DF of the critical sliding force for which Iwan
147 assumes a uniform distribution. This ratio is usually identified by matching with experimental data
148 and changes the shape of hysteresis curves during micro slip. Therefore, it can be seen that the DF
149 plays a key role in the Iwan model. In the next section, a novel approach is proposed that can directly
150 derive the Iwan DF from the contact pressure distribution on the joint surface, differently from what
151 is done in the Iwan-type models where the DF is assumed a priori regardless of the pressure
152 distribution.

153 **2.2 Modeling process**

154 Under tangential loads the contact surface shows two regions: a slip region in which corresponding
155 contact pairs on contact surfaces undergo a relative motion and a stick region in which the relative
156 motion is not allowed. As an example, on a sphere-on-sphere contact the slip region is the annular
157 periphery of the contact area, where the contact pressure is lower and is not able to constrain the
158 relative motion between contact pairs. Therefore, it is evident that the contact pressure plays an
159 important role in defining the motion state of contact pairs. If the DF of the critical sliding force is
160 related to pressure distribution, the obtained DF has an explicit physical significance and is no more
161 a sheer parameter in the model.

162

163 Fig. 2 illustrates in five steps the proposed approach. Step (1) assumes a contact pressure distribution
164 $p(x)$ from known analytical or semi-analytical solutions, measurements or empirical formulations,

$$p = p(N, x, a), \ |x| \leq a, \tag{3}$$

165 where a and N denote the size of contact area and the normal load, respectively. During the whole

process the contact pressure distribution is assumed independent of the relative motion.

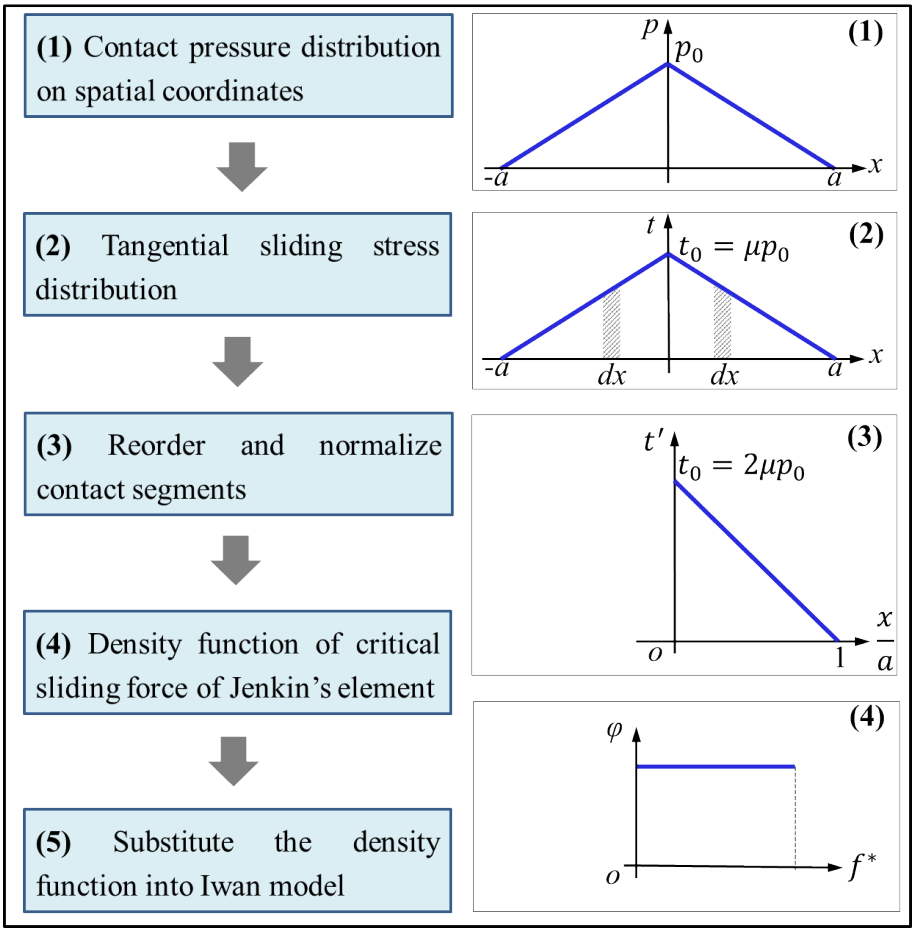

Fig. 2. Flow chart of the proposed modeling approach and an example of a "triangle" pressure distribution.

Step (2) builds the distribution function of the tangential sliding stress $t(x)$ (also denoted "*traction*") under the assumption that the Coulomb law between pressure $p(x)$ and traction $t(x)$ holds at infinitesimal level. In the case of slip on the whole contact area the distribution function of traction becomes,

$$t(x) = \mu\, p(N, x, a),\ |x| \le a. \tag{4}$$

Eq. (4) cannot simulate the microslip condition. The density function $\varphi(f^*)$ determines the

176 distribution of the critical value (or threshold) of the sliding force. This threshold defines the slip and
177 stick regions in the contact area, which in turn determine the real tangential force.
178
179 To illustrate the procedure a simple triangular distribution of contact pressure, symmetrical about the
180 x axis with p_0 the maximum pressure, has been considered, see Fig. 2. In step (3), contact segments
181 with the same tangential pressure have been sorted in descending order, to simplify the following
182 calculation. The sorting process does not change the total sliding force and the sorted traction
183 distribution $t^{'}$ is

$$t^{'}(x) = 2\mu p(N, x, a), \quad 0 \le x \le a. \tag{5}$$

184 The traction distribution $t^{'}(x)$ in the spatial domain is related to the distribution of traction f^* on
185 the Jenkins elements

$$f^* = a \cdot t^{'}(x). \tag{6}$$

186 From a statistical viewpoint, $\varphi(f^*)\mathrm{d}f^*$ is the probability that the critical sliding force falls within
187 the range f^* and $f^* + \mathrm{d}f^*$, namely the occurrence of the event f^* in the spatial domain

$$\varphi(f^*)\mathrm{d}f^* = \frac{\mathrm{d}x}{a}. \tag{7}$$

188 Then, the distribution density $\varphi(f^*)$ can be defined as the cotangent of the curve of the critical
189 sliding force

$$\varphi(f^*) = \frac{\mathrm{d}x}{a \cdot \mathrm{d}f^*}. \tag{8}$$

190 Step (5) uses the obtained DF into the Iwan model and gets the tangential force for monotonic and
191 cyclic loading cases by Eqs. (1) and (2).

192 **2.3 Parameter estimation method**

193 Compared with the original Iwan model, the proposed modeling approach does not involve
194 parameters related to the DF form, that is defined a priori. Therefore, the proposed model uses only
195 two parameters, related to the tangential stiffness and the friction coefficient. These parameters need
196 to be identified from experimental results.

197

198 It is well known that the tangential stiffness can be easily estimated through the force-displacement
199 curve, denoted as hysteresis loop, see Fig. 3. The slope of the curve in the initial state ("stick" state)
200 is the tangential stiffness, while, when the contact reaches a gross slip state, the ratio of tangential to
201 normal force is the friction coefficient.

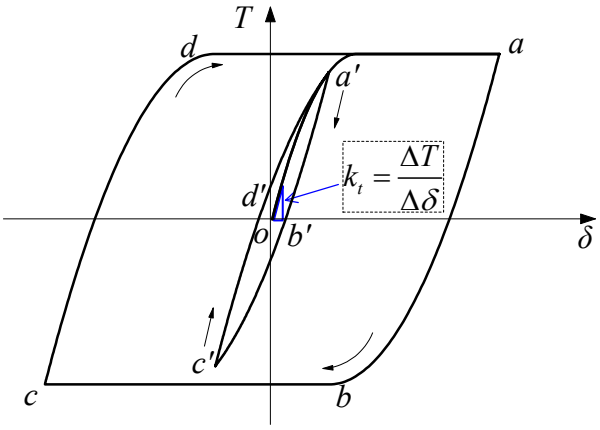

202

203 **Fig. 3.** Typical hysteresis loops for micro-slip and gross slip cases, and schematic of contact
204 stiffness.

205

3 Analytical validation in a sphere-on-sphere contact

In this section, the proposed approach is used to simulate the tangential force against the relative displacement in the friction contact between two elastic spheres. Results predicted by the model are compared with Mindlin analytical solution [31, 34] to validate the approach.

3.1 Mindlin analytical solution

Mindlin [31, 34] studied the friction contact of two elastic spheres pressed by a normal force N in which the contact area is circular with radius a. The contact area and pressure distribution on the surface are given by Hertz theory [27]. Mindlin results show that the contact area is divided into slip and stick region, the slip region being at the outer radius. The slip region increases with the tangential load. According to Mindlin, for a monotonic tangential loading case, the displacement-force relation on the contact surface is given as

$$\delta = \frac{3(2-\vartheta)\mu N}{16Ga}\left[1-\left(1-\frac{T}{\mu N}\right)^{2/3}\right] \tag{9}$$

where ϑ and G denote Poisson's ratio and shear modulus, respectively.

For a cyclic tangential loading case, the relationship between the tangential force and the relative displacement for the unloading and reloading are given as

$$\delta = \begin{cases} \dfrac{3(2-\vartheta)\mu N}{16Ga}\left[2\left(1-\dfrac{T_m - T}{2\mu N}\right)^{2/3} - \left(1-\dfrac{T_m}{\mu N}\right)^{2/3} - 1\right], & \dot{T} < 0, \\ -\dfrac{3(2-\vartheta)\mu N}{16Ga}\left[2\left(1-\dfrac{T_m + T}{2\mu N}\right)^{2/3} - \left(1-\dfrac{T_m}{\mu N}\right)^{2/3} - 1\right], & \dot{T} > 0, \end{cases} \tag{10}$$

where T_m is the maximum tangential force before reversal.

The curve depicted according to Eq. (10) can form a hysteresis loop. The area enclosed by the loop represents the dissipated energy per cycle

$$W = \frac{9(2-\vartheta)\mu^2 N^2}{10Ga}\left\{\left[1-\left(1-\frac{T_m}{\mu N}\right)^{5/3}\right] - \frac{5T_m}{6\mu N}\left[1+\left(1-\frac{T_m}{\mu N}\right)^{2/3}\right]\right\}. \tag{11}$$

For a small $T_m/\mu N$, Eq. (11) reduces to

$$W = \frac{(2-\vartheta)T_m^3}{36Ga\mu N}. \tag{12}$$

The dissipated energy is proportional to the cubic power of the maximum tangential load. It should be noted that this equation does not consider gross slip case and is valid only for small tangential loads.

3.2 Modeling sphere-on-sphere friction contact

According to the proposed approach the contact pressure distribution is assumed a priori, and this pressure is used to obtain the DF of the critical sliding force. For two elastic spheres in contact, the pressure distribution is given by Hertz theory [27], as shown in Fig. 4(a),

$$p(r) = p_0\sqrt{1-(r/a)^2}, \quad 0 \le r \le a, \tag{13}$$

where $p(r)$ is the contact pressure, r the distance from the center of contact area, and p_0 the maximum contact pressure $p_0 = 3N/(2\pi a^2)$.

The two-dimensional distribution is converted to an equivalent one-dimensional distribution along the x axis. This step is needed to describe the pressure distribution (given in spatial coordinates) in the Jenkins elements coordinates. To achieve this conversion, the contact pressure is integrated along the y axis to give the normal force per contact width

$$n_{\mathrm{eq}}(x) = \int_{-\sqrt{a^2-x^2}}^{\sqrt{a^2-x^2}} p_0 \sqrt{1-\left(\frac{x}{a}\right)^2-\left(\frac{y}{a}\right)^2}\,\mathrm{d}y = \frac{\pi p_0}{2a}(a^2-x^2), \tag{14}$$

In this process, the circular contact area becomes a one-dimensional contact region in the domain $-a \le x \le a$. Fig. 4(b) shows the normal force per contact width whose maximum value is $n_0 = \pi p_0 a/2$.

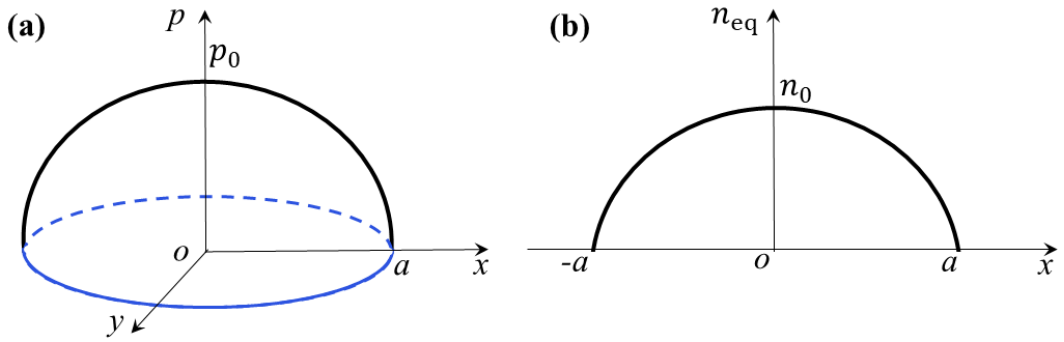

Fig. 4. Contact pressure distribution of two elastic spheres (a) on two-dimensional space, (b) on one-dimensional space.

The tangential sliding stress distribution in the slip case can be obtained by Coulomb law (see the step (2) in Fig. 2),

$$t(x) = \mu n_{\mathrm{eq}}(x) = \frac{\pi \mu p_0}{2a}(a^2-x^2),\ (-a \le x \le a). \tag{15}$$

Due to the symmetrical distribution of $t(x)$, contact segments with the same sliding stress can be sorted giving

$$t'(x) = \frac{\pi\mu p_0}{a}(a^2 - x^2),\ (0 \le x \le a). \tag{16}$$

252 Coordinates in the contact region are normalized, according to the step (3) in Fig. 2, and the sliding
253 stress distribution is written as

$$t'(x/a) = \pi\mu p_0 a\left[1 - \left(\frac{x}{a}\right)^2\right],\ \left(0 \le \frac{x}{a} \le 1\right). \tag{17}$$

254 The critical sliding force in the normalized contact coordinate is then

$$f^*(x/a) = a \cdot t'(x/a) = \pi\mu p_0 a^2\left[1 - \left(\frac{x}{a}\right)^2\right],\ \left(0 \le \frac{x}{a} \le 1\right). \tag{18}$$

255 Fig. 5(a) plots the dimensionless critical sliding force $f^*/\mu N$ vs. the dimensionless contact width
256 *x/a*. Solving Eq. (18) for *x/a*, considering that $p_0 = {}^{3N}/_{(2\pi a^2)}$, the following relationship is
257 obtained

$$\frac{x}{a} = \sqrt{1 - \frac{2f^*}{3\mu N}},\ \left(0 \le \frac{x}{a} \le 1\right). \tag{19}$$

258 Finally, the DF $\varphi(f^*)$ of the critical sliding force $f^*(x/a)$ is carried out according to its
259 definition

$$\varphi(f^*) = \left|\frac{\mathrm{d}(x/a)}{\mathrm{d}f^*}\right| = \frac{1}{\sqrt{3\mu N(3\mu N - 2f^*)}}. \tag{20}$$

260 Fig. 5(b) plots the dimensionless density function $\varphi(f^*)\mu N$ vs. the dimensionless critical sliding
261 force $f^*/\mu N$.

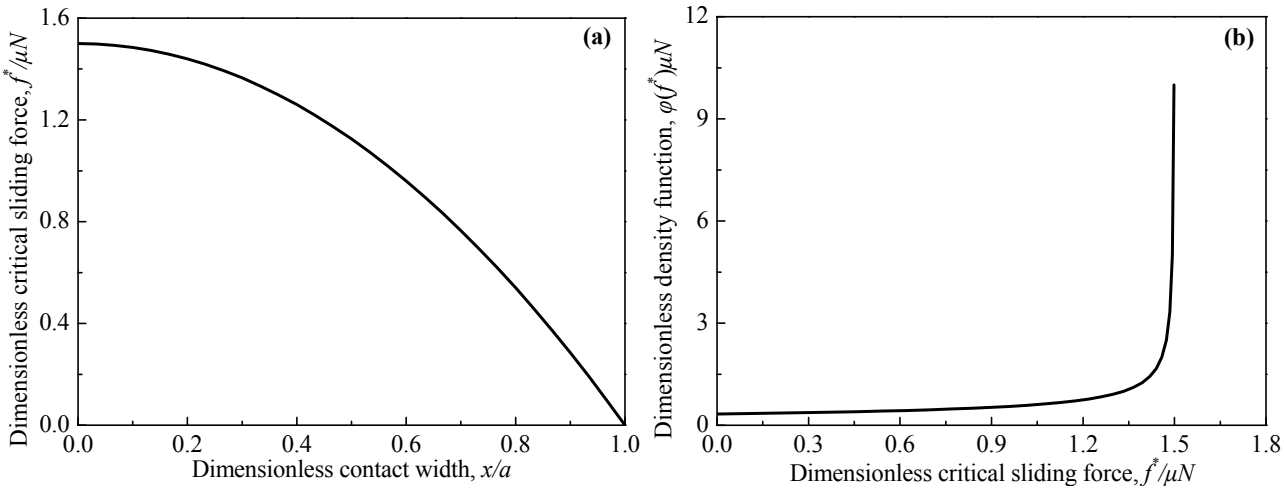

Fig. 5. (a) Dimensionless critical sliding force $f^*/\mu N$ vs. dimensionless contact width x/a; (b) Dimensionless density function $\varphi(f^*)\mu N$ vs. dimensionless critical sliding force $f^*/\mu N$.

Substituting Eq. (20) into Eq. (1) yields the tangential force,

$$T = \mu N - \frac{(3\mu N - 2k_t\delta)^{3/2}}{3\sqrt{3\mu N}}. \tag{21}$$

For a cyclic loading, the expression of the tangential force is obtained according to the Masing's hypothesis,

$$T(\delta) = \begin{cases} -T(\delta_m) + 2T\left(\dfrac{\delta_m + \delta}{2}\right), & \dot{\delta} > 0 \\ T(\delta_m) - 2T\left(\dfrac{\delta_m - \delta}{2}\right), & \dot{\delta} < 0 \end{cases}. \tag{22}$$

3.3 Comparison with analytical solution

The proposed approach has been applied to two identical elastic spheres in contact and the results have been compared with the Mindlin's analytical solution. Material properties, friction coefficient, contact radius and normal load used in the simulation are listed in Table 1.

Table 1 Analytical model parameters

Shear modulus	Poisson's ratio	Friction coefficient	Contact radius	Normal load
27GPa	0.33	0.5	2mm	500N

The tangential stiffness to be used in the model is the slope of force-displacement curve when the body are at rest and start moving. To be consistent, this stiffness has been computed using the Mindlin solution

$$k_t = \lim_{\delta \to 0} \frac{\partial T}{\partial \delta} = \lim_{\delta \to 0} \frac{8Ga}{2-\vartheta}\left[1 - \frac{16Ga\delta}{3(2-\vartheta)\mu N}\right]^{1/2} = \frac{8Ga}{2-\vartheta}, \tag{23}$$

A harmonic displacement δ was applied to one of the contact bodies to compute the tangential force T. Two cases were studied: a small relative displacement for which the sliding condition is not reached (maximum tangential force $T_m < \mu N = 200$N) and a large relative displacement up to full sliding conditions (maximum tangential force $T_m = \mu N = 250$N). Fig. 6 shows that the proposed method is equivalent to the Mindlin's analytical solution; as can be easily verified by substituting Eq. (23) into Eq. (21).

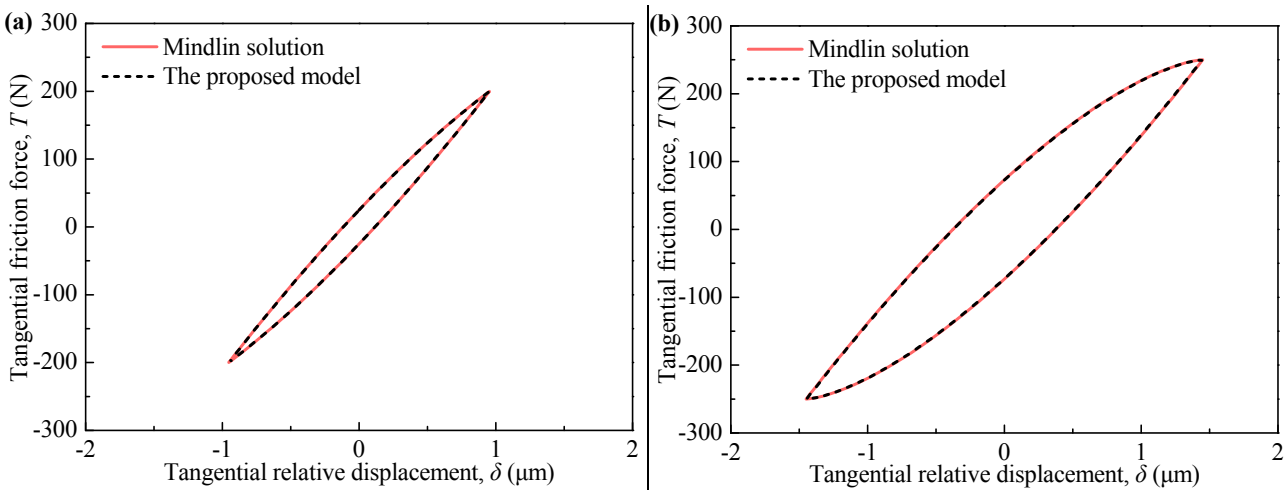

Fig. 6. Comparison of hysteresis loops predicted by the proposed model with Mindlin solution, (a) $T_m = 200$N; (b) $T_m = 250$N.

Fig. 7 compares the dissipated energy per cycle and confirms the equivalence of the two methods. The proposed model can also be used to simulate friction behavior for several contact geometries. In the next section, two flat contact bodies will be modeled with the proposed approach and compared with experimental data.

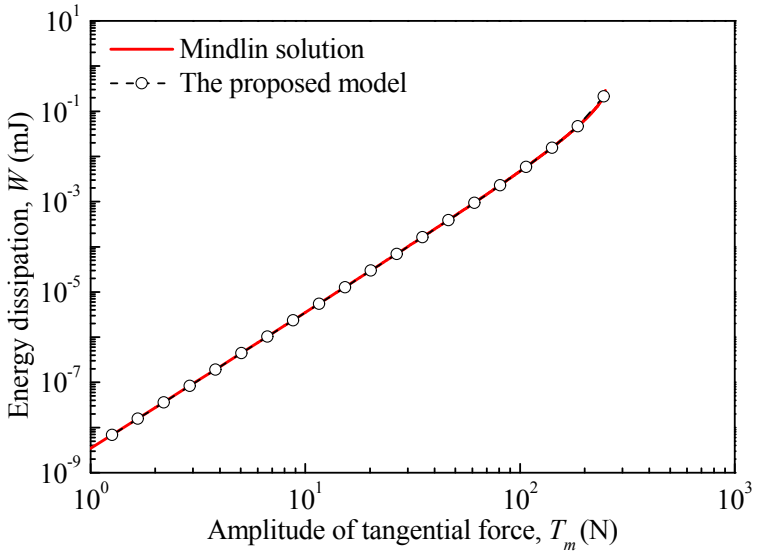

Fig. 7. Comparison of predicted energy dissipation per cycle with Mindlin's solution.

4 Modeling friction for lap joint plates

Lap joints are unavoidable in assembled structures such as bolted and riveted joints. Friction contact at the joint interfaces has a significant effect on the dynamic behavior of assembled structures, in which non-linearities originate at the contact. Therefore, the development of a reliable friction model for flat-on-flat contact can contribute to accurately predict the forced-responses of these structures. In this section, the proposed approach is used to simulate contact behavior in lap joints and then validated by comparison with measured results.

4.1 Representation of friction between lap joints

It is challenging to obtain a distribution function of contact pressure for flat-on-flat contact because of asperities and waviness that affect the real contact area. Moreover, cyclic loading modifies the contact because surfaces change their topography and pressure is redistributed on the contact area. These phenomena, more evident in flat contact than in point contact, could limit the application of the proposed model.

To overcome this limit, a quadratic function with a variable parameter ω was assumed to describe the distribution function of the contact pressure. This variable parameter was denoted 'proportional coefficient' and defined as the ratio between the peak pressure p_0 and the mean pressure p_m

$$\gamma = \frac{p(0)}{N/aw}. \tag{24}$$

This quadratic function can represent three typical distribution forms widely employed to approximate real cases, namely "concave", "convex", and "uniform" distribution [13]. According to

316 the proposed approach, a unified friction model including the variable parameter is developed for
317 flat-on-flat contact. The optimal choice of this parameter can be inferred from the measured
318 hysteresis loops.
319
320 Fig. 8 shows two plates pressed together by a normal load N and excited by an oscillating tangential
321 displacement δ. The nominal contact area length is a. The cross section of the plate is a rectangle of
322 width w and thickness h. The normal load along the transverse direction is assumed to be uniformly
323 distributed.

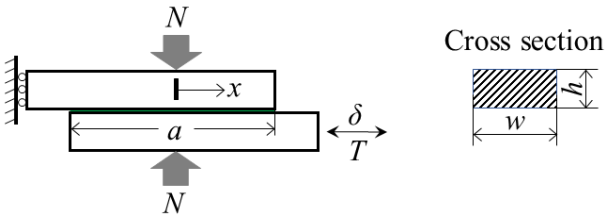

324
325 **Fig. 8.** Lap joint plates model and cross section of the plate
326
327 In this paper, we define the quadratic function assuming that i) the real contact area is the nominal
328 contact area and ii) the extreme value of the quadratic function is in the center of the contact area

$$p(x) = \frac{N}{aw}\left[\frac{12(1-\gamma)x^2}{a^2} + \gamma\right], \left(x \le \left|\frac{a}{2}\right|\right) \tag{25}$$

329 where γ is the proportional coefficient varying in the range [0, 1.5]. For the case $\gamma < 1$, Eq. (25) is a
330 concave distribution function, while for the case $\gamma > 1$, it is a convex distribution function.
331 Proportional coefficient $\gamma = 1$ means that the distribution of contact pressure is constant. Fig. 9
332 shows dimensionless contact pressure, $p(x)aw/N$, against the normalized contact coordinate, x/a,
333 for different proportional coefficients. For a real lap joint, the corresponding pressure distribution

function is approximately represented by selecting a suitable proportional coefficient.

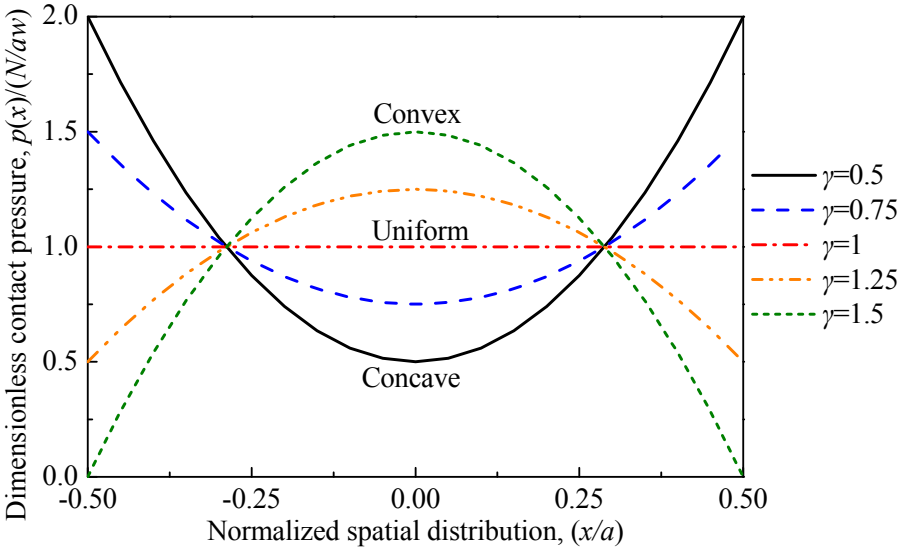

Fig. 9. Dimensionless contact pressure distribution, $p(x)aw/N$, vs. normalized contact coordinate, x/a, for different proportional coefficients.

According to the proposed model, section 2, the tangential sliding stress distribution can be derived as

$$t(x) = \mu p(x) = \frac{\mu N}{aw}\left[\frac{12(1-\gamma)x^2}{a^2} + \gamma\right], \left(x \le \left|\frac{a}{2}\right|\right). \tag{26}$$

Then, the distribution function is reordered, and the spatial coordinate normalized,

$$t'(2x/a) = \frac{2\mu N}{aw}\left[3(1-\gamma)\left(\frac{2x}{a}\right)^2 + \gamma\right], \left(0 \le \frac{2x}{a} \le 1\right). \tag{27}$$

The critical sliding force in the normalized contact coordinate is

$$f^*(2x/a) = \frac{aw}{2} \cdot t'\left(\frac{2x}{a}\right) = \mu N\left[3(1-\gamma)\left(\frac{2x}{a}\right)^2 + \gamma\right]. \tag{28}$$

According to the definition of the Iwan DF in Eq. (8), it can be obtained by deriving the normalized contact coordinate with respect to the critical sliding force,

$$\varphi(f^*) = \left|\frac{\mathrm{d}(2x/a)}{\mathrm{d}f^*}\right| = \frac{1}{2\mu N\sqrt{3(1-\gamma)\left(\frac{f^*}{\mu N}-\gamma\right)}}. \tag{29}$$

Fig. 10 shows a group of dimensionless density functions of critical sliding force $\varphi(f^*)$ with different proportional coefficients. For the concave distribution, the DF goes to infinity when the critical sliding force approaches its minimum, $\gamma\mu N$, whereas for the convex distribution, the DF goes to infinity when the critical sliding force approaches its maximum, $\gamma\mu N$.

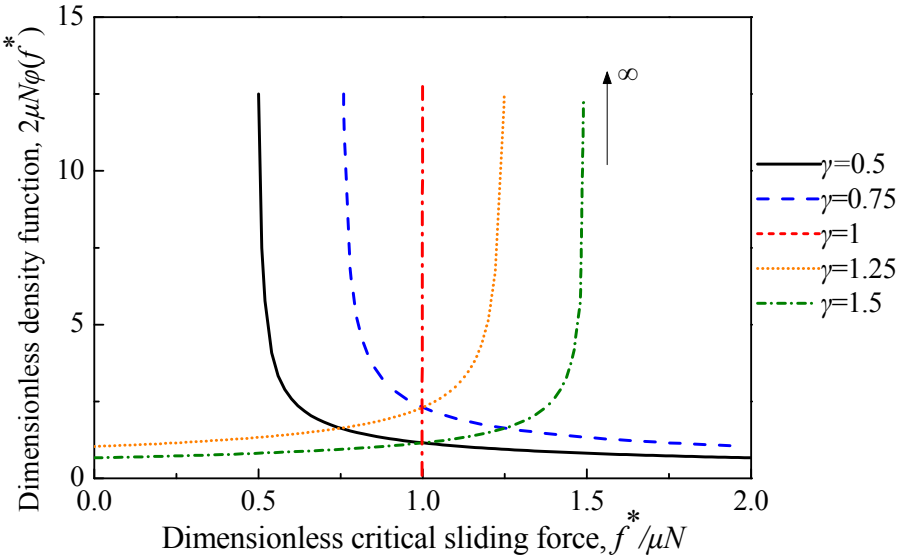

Fig. 10 Dimensionless density function, $2\mu N\varphi(f^*)$, vs. dimensionless critical sliding force, $f^*/\mu N$, for different proportional coefficients.

The force-displacement expression is obtained from integral in Eq. (1)

$$T(\delta) = \int_{lb}^{k_t\delta} f^*\varphi(f^*)\mathrm{d}f^* + k_t\delta\int_{k_t\delta}^{ub}\varphi(f^*)\mathrm{d}f^*. \tag{30}$$

setting the proper upper and lower bounds that are different between the concave and convex distributions and are listed in Table 2. Details can be found in **Appendix A**.

Table 2. Upper and lower bounds of the concave and convex distributions, and corresponding force-displacement expressions

Concave distribution ($\gamma < 1$)	Convex distribution ($\gamma > 1$)
$lb = \gamma\mu N, ub = (3-2\gamma)\mu N$	$lb = (3-2\gamma)\mu N, ub = \gamma\mu N$
$T(\delta) = k_t\delta, \left(\delta \le \frac{\gamma\mu N}{k_t}\right)$	$T(\delta) = k_t\delta, \left(\delta \le \frac{(3-2\gamma)\mu N}{k_t}\right)$
$T(\delta) = k_t\delta + \frac{2(\gamma\mu N - k_t\delta)}{3}\sqrt{\frac{k_t\delta - \gamma\mu N}{3(1-\gamma)\mu N}}, \left(\frac{\gamma\mu N}{k_t} < \delta \le \frac{(3-2\gamma)\mu N}{k_t}\right)$	$T(\delta) = \mu N - \frac{2(\gamma\mu N - k_t\delta)}{3}\sqrt{\frac{k_t\delta - \gamma\mu N}{3(1-\gamma)\mu N}}, \left(\frac{(3-2\gamma)\mu N}{k_t} < \delta \le \frac{\gamma\mu N}{k_t}\right)$
$T(\delta) = \mu N, \left(\delta > \frac{(3-2\gamma)\mu N}{k_t}\right)$.	$T(\delta) = \mu N, \left(\delta > \frac{\gamma\mu N}{k_t}\right)$.

4.2 Model validation

Hysteresis loops measured on flat-on-flat contacts have been used to extract the contact parameters (namely tangential stiffness k_t, friction coefficient μ, residual stiffness coefficient α and proportional coefficient γ) and to validate the proposed model. Details of the test rig and experimental operation can be found in [35, 36]. Fig. 11 shows the specimens, denoted to as Fixed and Mobile respectively, used in the experimental tests and the corresponding contact area.

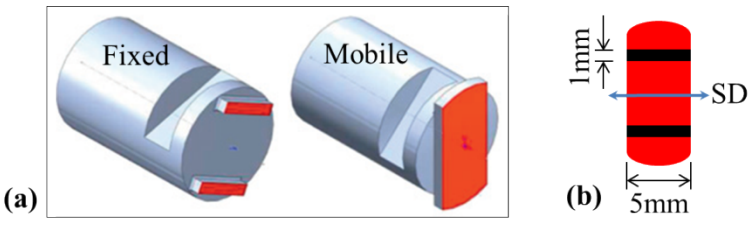

Fig. 11. (a) Specimens and contact surface of fretting tests, (b) contact area in black and sliding direction (SD).

Three cases, with different normal loads 87 N, 164 N and 254 N, were tested. Fig.12 shows typical measured hysteresis loops, in blue solid line, during ten periods. The three stages (Ⅰ) stick, (Ⅱ) micro-slip, and (Ⅲ) gross slip are indicated in the loops. The slope of the stick portion is regarded as the tangential stiffness. The friction coefficient is extracted from the ratio of tangential force over normal force at the onset of the gross slip stage. The residual stiffness coefficient is expressed as the ratio of the slope of the gross slip portion over the tangential stiffness. The proportional coefficient, used to effectively reproduce micro-slip, can be estimated with the best fit on the measured loop. All estimated parameters are listed in Table 3. Results illustrate the three normal loads share the same proportional coefficient in this experiment. Fig. 12 shows the comparison between the simulated and the experimental hysteresis loops with the proposed model. It can be seen that simulations match well with experimental results. Figure 12(a) shows that there are slight differences between the simulation and the experiment when the load is reversed. This is due to the inconsistent tangential stiffness during the loading and unloading phases, which sometimes occurs in the test. Figure 12(b and c) shows that there are two uncommon bulges in the measured hysteresis loops. The first one occurred at the transition from the stuck to the micro-slip state. This may be caused by local interactions between the asperities on contact surfaces. The second occurred at the end of the gross slip stage. This phenomenon has been observed in many tests [35, 37, 38], however, the physical reason for it is not yet fully understood. Two possible reasons are “velocity effect” and interactions at contact edges. These uncommon behaviors observed in the experiment were not captured by the proposed method.

Due to the existence of waviness and roughness of contact surfaces, it is difficult to analytically obtain the contact pressure distribution of flat-on-flat contact. Besides, the dispersion of contact pressure distribution by measurement may be significant. Even so, the obtained Iwan DF based on a quadratic distribution depending on a proportional coefficient can give satisfactory results. This is a more practical application of the proposed method.

Table 3 Applied normal loads and estimated contact parameters in tests

Normal load, N (N)	Tangential stiffness, k_t (N/μm)	Residual stiffness coefficient, α	Friction coefficient, μ	Proportional coefficient, γ
87	30.5	0.0427	0.48	0.2
164	113.7	0	0.68	0.2
254	133.7	0.0445	0.65	0.2

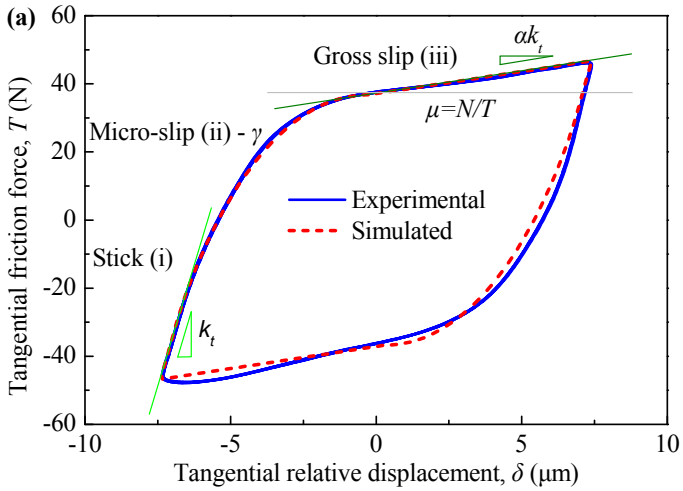

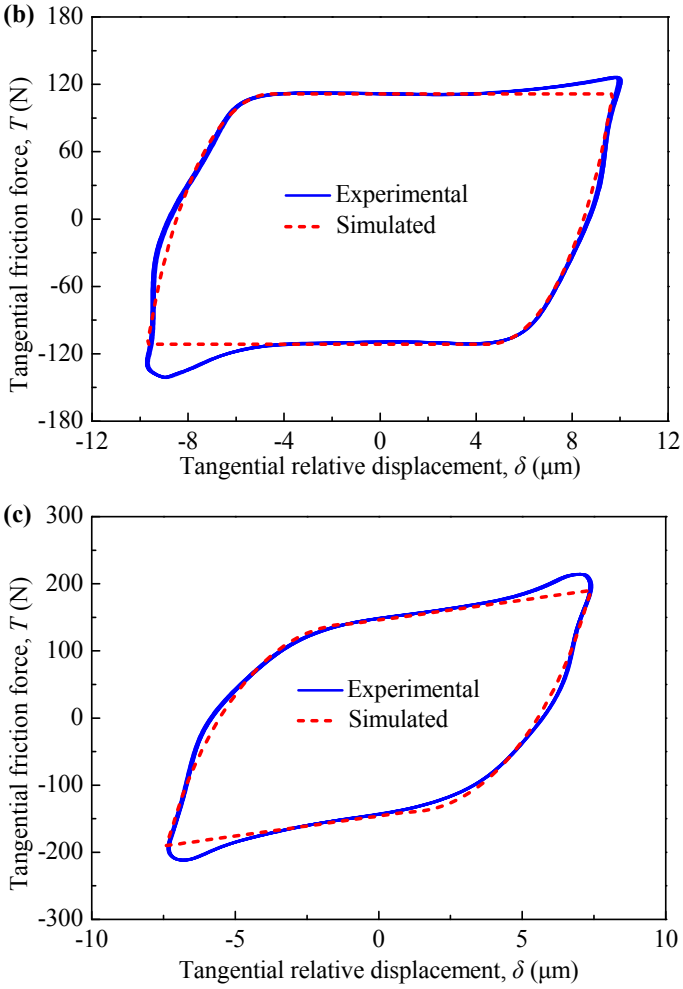

Fig. 12. Comparison between numerical and experimental hysteresis loops for two normal loads, (a) N=87 N, (b) N=164N, (c) N=254N.

4.3 Effect of the proportional coefficient

The proposed contact model introduces a proportional coefficient whose range varies in the range [0, 1.5]. The effect of this proportional coefficient is to change the shape of the hysteresis loop, then modelling different contacts. To study the effect that the proportional coefficient has on the hysteresis loops a normalization procedure is introduced. The relative displacement and tangential friction force are normalized as $\delta_{\text{norm}} = {}^{\delta}/_{\delta_{\text{max\_stick}}} = {}^{k_t\delta}/_{\mu N}$ and $T_{\text{norm}} = {}^{T}/_{\mu N}$. The obtained dimensionless backbone function is then

$$T_{\text{norm}} = \begin{cases} \delta_{\text{norm}} + \dfrac{2(\gamma - \delta_{\text{norm}})}{3}\sqrt{\dfrac{\delta_{\text{norm}} - \gamma}{3(1-\gamma)}}, & 0 \le \gamma \le 1 \\ 1 - \dfrac{2(\gamma - \delta_{\text{norm}})}{3}\sqrt{\dfrac{\delta_{\text{norm}} - \gamma}{3(1-\gamma)}}, & 1 < \gamma \le 1.5 \end{cases} . \tag{31}$$

Fig. 13 shows a group of dimensionless hysteresis loops with different proportional coefficients and the same others contact parameters. The imposed displacement is a sinusoidal motion with a normalized amplitude of 2 and a frequency of 1 Hz. It is evident that the proportional coefficient controls the micro-slip region and the global shape of hysteresis loops. When $\gamma < 1$, the predicted micro-slip effect gradually weakens as the proportional coefficient increases. While it is opposite when $\gamma > 1$.

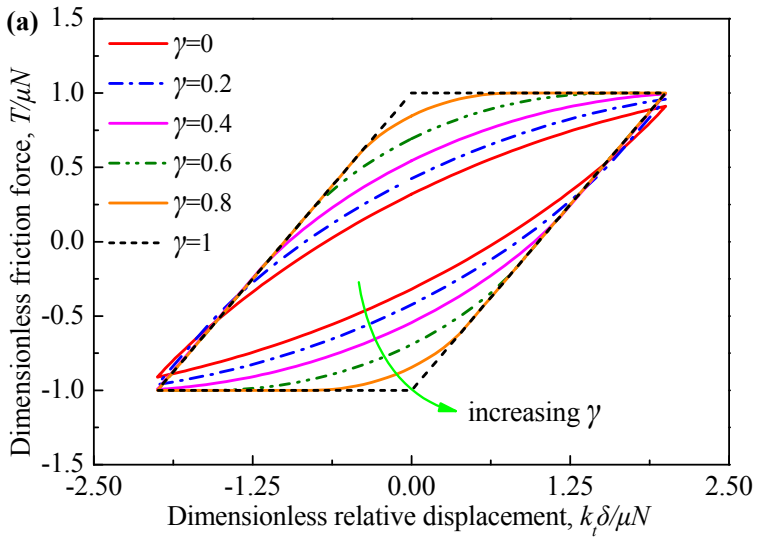

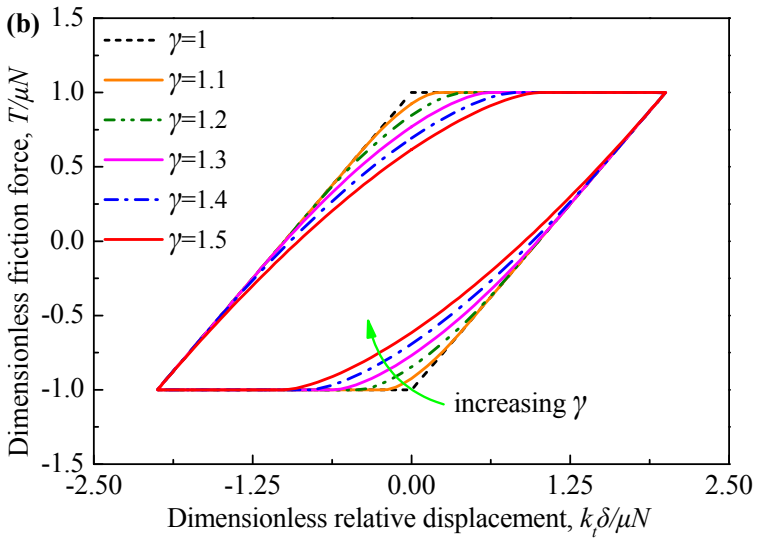

Fig. 13. Evolution of hysteresis loops (dimensionless friction force $T/\mu N$ vs. dimensionless relative displacement $k_t\delta/\mu N$) with the increase of proportional coefficient γ, (a) γ in the range [0, 1]; (b) γ in the range [1, 1.5].

Correspondingly, the proportional coefficient has an influence on the dissipated energy per cycle. Fig. 14 depicts the evolution of the normalized energy dissipated (enclosed area divided by its maximum value) with increasing the proportional coefficient under different displacement amplitudes. The normalized energy dissipated is not monotonic and shows dependence on amplitudes of displacement. For a relatively small displacement amplitude, there is a bandwidth of the proportional coefficient at which the corresponding model predicts zero energy dissipation. In this case, the stuck regime dominates the motion of contact surfaces. And the smaller the displacement amplitude, the wider this bandwidth. While for a relatively larger displacement amplitude, the energy dissipation shows a maximum when γ=1. As the proportional coefficient increases, the normalized energy dissipated increases first and then drops slightly. In addition, the difference in the dissipated energy among different proportional coefficient decreases with the increasing proportional coefficient. This is due to the gradual dominance of the gross slip regime.

From a certain point of view, the proposed method is a generalized Iwan model, which starts with the contact pressure distribution and shows how to derive the Iwan DF. In applications where it is difficult to obtain the pressure distribution function, the proportional coefficient, which indirectly reflects the pressure distribution, can be easily estimated from experimental results.

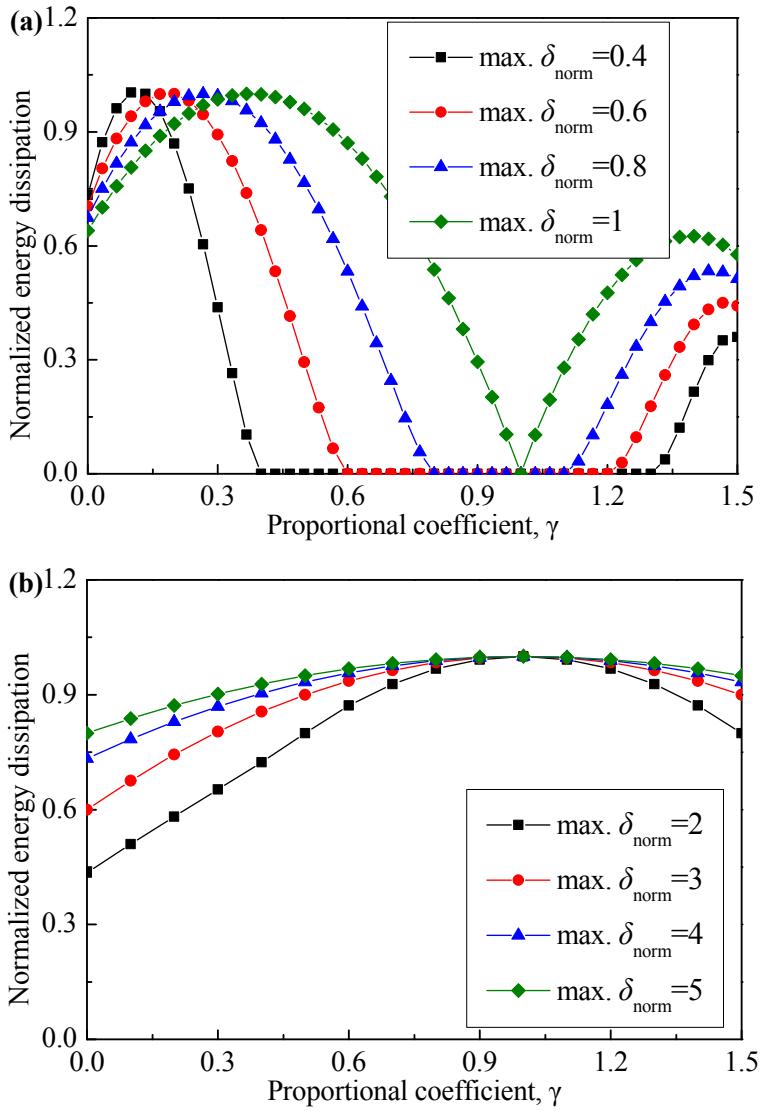

441

442

443 **Fig. 14.** Normalized energy dissipation (enclosed area divided by its maximum value) vs.

444 proportional coefficient γ under different displacement amplitudes.

445

5 Conclusions

This work presents a new friction modeling approach based on the framework of the original Iwan's model. The aim of this new approach is to better describe the relationship between the friction force and the relative displacements. The proposed approach was employed to simulate the friction behavior of a sphere-on-sphere contact in which the pressure distribution has been assumed as in the Hertzian contact. The approach was validated by comparison with the Mindlin's analytical solution. In addition, the approach was applied to a flat-on-flat contact of lap joints where the pressure distribution is known with great approximation. A proportional coefficient is introduced, which controls the micro-slip region and the global shape of hysteresis loops.

The application of this method to contacts with different normal loads showed a great variation of the contact parameters such as contact stiffness, friction coefficient, and residual stiffness. On the other hand, the proportional coefficient remained the same or showed a non-appreciable variation. The main outcome of this paper is that even if the pressure distribution is not known, for the specific contact, it can be replaced by the density function whose distribution is well represented with the proportional coefficient. Experimental evidence has shown that the proportional coefficient, that is related to the density function distribution, remains constant for contacts with the same geometry but different contact conditions. The method described in this paper is then useful for improving the prediction performance of dynamics of jointed structures in many engineering applications and for the optimal design of components of assemblies, and to simulate wear between contact surfaces.

Acknowledgments

The authors wish to acknowledge and thank the China Science Challenge for funding their research project (TZ2018007). Dongwu Li would also like to show his gratitude to China Scholarship Council (CSC) for supporting him as visiting PhD to AERMEC lab of Politecnico di Torino within the project EXTHENdED.

Declaration of interests

The authors declare that they have no conflicts of competing interests.

476 # Appendix A

477 Considering the upper and lower bounds (the integral limits in Eq. (1)) of critical sliding force are
478 different between the concave and convex distributions, the corresponding force-displacement
479 expressions are derived respectively. For the concave distribution, the critical sliding force falls
480 within the range $[\gamma\mu N, (3-2\gamma)\mu N]$. When the relative displacement is lower than $\gamma\mu N/k_t$, all
481 Jenkins elements are in stick state. That is, the recovery force behaves linearly with respect to
482 relative displacement,

$$T(\delta) = k_t\delta, \left(0 < \delta \le \frac{\gamma\mu N}{k_t}\right) \tag{A.1}$$

483 When the relative displacement falls with the range $[\gamma\mu N/k_t, (3-2\gamma)\mu N/k_t]$, the recovery force is
484 obtained by substituting the DF into Eq. (1),

$$\begin{aligned} T(\delta) &= \int_{\gamma\mu N}^{k_t\delta} f^* \varphi(f^*) df^* + k_t\delta \int_{k_t\delta}^{(3-2\gamma)\mu N} \varphi(f^*) df^* \\ &= k_t\delta + \frac{2(\gamma\mu N - k_t\delta)}{3}\sqrt{\frac{\frac{k_t\delta}{\mu N} - \gamma}{3(1-\gamma)}}, \left(\frac{\gamma\mu N}{k_t} < \delta \le \frac{(3-2\gamma)\mu N}{k_t}\right). \end{aligned} \tag{A.2}$$

485 When the relative displacement is larger than $(3-2\gamma)\mu N/k_t$, all Jenkins elements are in slip state
486 and the recovery force equals μN.

487

488 For the convex distribution, the critical sliding force falls within the range $[(3-2\gamma)\mu N, \gamma\mu N]$.
489 When the relative displacement is lower than $(3-2\gamma)\mu N/k_t$, the recovery force is

$$T(\delta) = k_t\delta, \left(0 < \delta \le \frac{(3-2\gamma)\mu N}{k_t}\right). \tag{A.3}$$

When the relative displacement falls with the range $[(3-2\gamma)\mu N/k_t,\ \gamma\mu N/k_t]$, the recovery force is

$$T(\delta) = \int_{(3-2\gamma)\mu N}^{k_t\delta} f^*\varphi(f^*)df^* + k_t\delta\int_{k_t\delta}^{\gamma\mu N}\varphi(f^*)df^*$$
$$= \mu N - \frac{2(\gamma\mu N - k_t\delta)}{3}\sqrt{\frac{\frac{k_t\delta}{\mu N}-\gamma}{3(1-\gamma)}},\ \left(\frac{(3-2\gamma)\mu N}{k_t} < \delta \le \frac{\gamma\mu N}{k_t}\right). \quad (A.4)$$

Similarly, when the relative displacement is larger than $\gamma\mu N/k_t$, the model is in gross slip state and the recovery force equals μN. For cyclic loadings, the force-displacement relation can be obtained by Masing hypothesis.

References

[1] Gaul L, Nitsche R. The role of friction in mechanical joints. Appl. Mech. Rev. 2001; 54: 93-106. https://doi.org/10.1115/1.3097294

[2] Gaul L, Lenz J. Nonlinear dynamics of structures assembled by bolted joints. Acta Mech. 1997;125: 169-181. https://doi.org/10.1007/BF01177306

[3] De Benedetti M, Garofalo G, Zumpano M, et al. On the damping effect due to bolted junctions in space structures subjected to pyro-shock. Acta Astronaut. 2007; 60: 947-956. https://doi.org/10.1016/j.actaastro.2006.11.011

[4] Feeny B, Guran A, Hinrichs N, et al. A historical review on dry friction and stick-slip phenomena. Appl. Mech. Rev. 1998; 51(5): 321-341. https://doi.org/10.1115/1. 3099008

[5] Yan Y, Xu J, Wiercigroch M. Modelling of regenerative and frictional cutting dynamics. Int. J. Mech. Sci. 2019; 156: 86-93. https://doi.org/10.1016/j.ijmecsci.2019.03.032

[6] Saha A, Wiercigroch M, Jankowski K, et al. Investigation of two different friction models from the perspective of friction-induced vibrations. Tribol. Int. 2015; 90: 185-197. https://doi.org/10.1016/j.triboint.2015.04.029

[7] Vaziri V, Kapitaniak M, Wiercigroch M. Suppression of drill-string stick–slip vibration by sliding mode control: Numerical and experimental studies. Eur. J. Appl. Math. 2018; 29(5): 805-825. https://doi.org/10.1017/S0956792518000232

[8] Bograd S, Reuss P, Schmidt A, et al. Modeling the dynamics of mechanical joints. Mech. Syst. Signal Process. 2011; 25: 2801-2826. https://doi.org/10.1016/j.ymssp.2011. 01.010

[9] Segalman DJ. A four-parameter Iwan model for lap-type joints. J. Appl. Mech. 2005; 72: 752-760. https://doi.org/10.1115/1.1989354

[10] Iwan WD. A distributed-element model for hysteresis and its steady-state dynamic response, J. Appl. Mech. 1966; 33: 893-900. https://doi.org/10.1115/1.3625199

[11] Iwan WD. On a class of models for the yielding behavior of continuous and composite systems. J. Appl. Mech. 1967; 34: 612-617. https://doi.org/10.1115/1.3607751

[12] Abad J, Medel FJ, Franco JM. Determination of Valanis model parameters in a bolted lap joint: Experimental and numerical analyses of frictional dissipation. Int. J. Mech. Sci. 2014; 89: 289-298. https://doi.org/10.1016/j.ijmecsci.2014.09.014

[13] Dahl PR. Solid friction damping of mechanical vibrations. AIAA journal, 1976; 14: 1675-1682. https://doi.org/10.2514/3.61511.

[14] Piatkowski T. Dahl and LuGre dynamic friction models—The analysis of selected properties. Mech. Mach. Theory. 2014; 73: 91-100. https://doi.org/10.1016/j.mechmachtheory. 2013.10.009

[15] Menq CH, Bielak J, Griffin JH. The influence of microslip on vibratory response, part I: a new microslip model. J. Sound Vib. 1986; 107: 279-293. https://doi.org/10.1016/0022-460X(86)90238-5

[16] Oldfield M, Ouyang H, Mottershead JE, Simplified models of bolted joints under harmonic loading. Comput. Struct. 2005; 84: 25-33. https://doi.org/10.1016/j.compstruc.2005.09.007

[17] Cigeroglu E, Lu W, Menq CH. One-dimensional dynamic microslip friction model. J. Sound Vib. 2006; 292: 881-898. https://doi.org/10.1016/j.jsv.2005.09.019

[18] Gastaldi C, Gola MM. On the relevance of a microslip contact model for underplatform

dampers. Int. J. Mech. Sci. 2016; 115: 145-156. https://doi.org/10.1016/j.ijmecsci.2016.06.015
[19] Argatov II, Butcher EA. On the Iwan models for lap-type bolted joints. Int. J. Non-Linear Mech. 2011; 46: 347-356. https://doi.org/10.1016/j.ijnonlinmec.2010.09. 018
[20] Zhan W, Huang P. Physics-based modeling for lap-type joints based on the Iwan model. J. Tribol. 2018; 140: 051401. https://doi.org/10.1115/1.4039530
[21] Segalman DJ, Starr MJ. Inversion of Masing models via continuous Iwan systems. Int. J. Non-Linear Mech. 2008; 43: 74-80. https://doi.org/10. 1016/j.ijnonlinmec.2007.10.005
[22] Song Y, Hartwigsen CJ, McFarland DM, et al. Simulation of dynamics of beam structures with bolted joints using adjusted Iwan beam elements. J. Sound Vib. 2004; 273: 249-276. https://doi.org/10.1016/S0022-460X(03)00499-1
[23] Wang D, Xu C, Fan X, Wan Q. Reduced-order modeling approach for frictional stick-slip behaviors of joint interface. Mech. Syst. Signal Process. 2018; 103: 131-138. https://doi.org/10.1016/j.ymssp.2017.10.001
[24] Li Y, Hao Z. A six-parameter Iwan model and its application. Mech. Syst. Signal Process. 2016; 68: 354-365. https://doi.org/10.1016/j.ymssp.2015.07.009.
[25] Li Y, Hao Z, Feng J, Zhang D. Investigation into discretization methods of the six-parameter Iwan model. Mech. Syst. Signal Process. 2017; 85: 98-110. https://doi.org/10.1016/j.ymssp.2016. 07.032.
[26] Brake MRW. A reduced Iwan model that includes pinning for bolted joint mechanics. Nonlinear Dyn. 2017; 87: 1335-1349. https://doi.org/10.1007/s11071-016- 3117-2
[27] Johnson KL. Contact mechanics. Cambridge university press, UK, 1987.
[28] Rajaei M, Ahmadian H. Development of generalized Iwan model to simulate frictional contacts with variable normal loads. Appl. Math. Model. 2014; 38: 4006-4018. https://doi.org/10.1016/j.apm.2014.01.008
[29] Li D, Xu C, Liu T, et al. A modified IWAN model for micro-slip in the context of dampers for turbine blade dynamics. Mech. Syst. Signal Process. 2019; 121: 14-30. https://doi.org/10.1016/j.ymssp.2018.11.002.
[30] Li D, Botto D, Xu C, et al. A micro-slip friction modeling approach and its application in underplatform damper kinematics. Int. J. Mech. Sci. 2019; 161-162: 105029. https://doi.org/10.1016/j.ijmecsci.2019.105029.
[31] Mindlin RD, Mason WP, Osmer TF, et al. Effects of an oscillating tangential force on the contact surfaces of elastic spheres. J. Appl. Mech. 1951; 18: 331-331. https://doi.org/10.1007/978-1-4613-8865-4_32
[32] Eriten M, Polycarpou AA, Bergman LA. Effects of surface roughness and lubrication on the early stages of fretting of mechanical lap joints. Wear. 2011; 271(11-12): 2928-2939. https://doi.org/10.1016/j.wear.2011.06.011
[33] Jenkins GM. Analysis of the stress–strain relationships in reactor grade graphite. Br. J. Appl. Phys. 1962; 13: 30–32. https://doi.org/10.1088/0508-3443/13/1/307
[34] Mindlin RD. Elastic spheres in contact under varying oblique forces. J. Applied Mech., 1953; 20: 327-344.
[35] Lavella M, Botto D. Fretting wear characterization by point contact of nickel superalloy interfaces. Wear, 2011; 271: 1543-1551. https://doi.org/10.1016/j.wear.2011.01.064.

578 [36] Botto D. Campagna A, Lavella M, Gola MM. Experimental and numerical investigation of
579 fretting wear at high temperature for aeronautical alloy. ASME. Turbo Expo 2010: Power for
580 Land, Sea, and Air, Volume 6. 1353-1362. https://doi.org/10.1115/GT2010-23356.
581 [37] Mulvihill DM, Kartal ME, Olver AV, et al. Investigation of non-Coulomb friction behaviour in
582 reciprocating sliding. Wear, 2011; 271(5-6): 802-816.
583 https://doi.org/10.1016/j.wear.2011.03.014
584 [38] Kartal ME, Mulvihill DM, Nowell D, et al. Measurements of pressure and area dependent
585 tangential contact stiffness between rough surfaces using digital image correlation. Tribol. Int.
586 2011; 44(10): 1188-1198. https://doi.org/10.1016/j.triboint.2011.05.025